



## Article

# Geochronology and Geochemistry of Archean TTG and Tremolite Schist Xenoliths in Yemadong Complex: Evidence for $\geq 3.0$ Ga Archean Continental Crust in Kongling High-Grade Metamorphic Terrane, Yangtze Craton, China

Yunxu Wei <sup>1,2,3</sup>, Wenxiao Zhou <sup>4,\*</sup> , Zhengxiang Hu <sup>5</sup>, Haiquan Li <sup>4</sup> , Xianxiao Huang <sup>4,6</sup>, Xiaoming Zhao <sup>1,2</sup> and Daliang Xu <sup>1,2</sup>

<sup>1</sup> Wuhan Center of China Geological Survey, Wuhan 430205, China; wyx1856@163.com (Y.W.); zxm20040021@163.com (X.Z.); Xdl2003geo@163.com (D.X.)

<sup>2</sup> Central South China Innovation Center for Geosciences, Wuhan 430205, China

<sup>3</sup> Research Center of Granitic Diagenesis and Mineralization, China Geological Survey, Wuhan 430205, China

<sup>4</sup> Institute of Geological Survey, China University of Geosciences, Wuhan 430074, China; lhq@cug.edu.cn (H.L.); huangxianxiao@outlook.com (X.H.)

<sup>5</sup> Hubei Geological Survey, Wuhan 430034, China; huzx111315@163.com

<sup>6</sup> Guangxi Regional Geological Survey, Guilin 541001, China

\* Correspondence: zhouwenxiao@cug.edu.cn; Tel.: +86-2767883017

Received: 28 September 2019; Accepted: 29 October 2019; Published: 8 November 2019



**Abstract:** The origin and significance of the tonalite–trondjemite–granodiorite (TTG) units and the familiar metabasite xenoliths they host in the Yangtze Craton, China, remain controversial, and resolving these issues is important if we are to understand the evolution of the early Yangtze Craton. We focused on biotite–tremolite schist xenoliths in the Archean TTG units of the Kongling high-grade metamorphic terrane, and U–Pb dating of their zircons yielded  $^{207}\text{Pb}/^{206}\text{Pb}$  ages of ca. 3.00 Ga, which provides a minimum age for the formation of the pre-metamorphic basic igneous rock. The host TTGs and late intrusive granitic dikes yield three groups of upper intercept ages at 2.87–2.88, 2.91–2.94, and 3.07 Ga, and a concordant age at 2.94 Ga, which suggest that the Yangtze continental nucleus underwent three important metamorphic–magmatic events in the Mesoarchean at ca. 3.00, 2.94, and 2.87 Ga. The biotite–tremolite schists have high ratios of  $\text{K}_2\text{O}/\text{Na}_2\text{O}$  and high contents of CaO, Cr, and Ni, thus showing the characteristics of high-K calc-alkaline island-arc volcanic rocks (basalt–andesite) that form by the partial melting of subducted oceanic crust. The data also provide further proof that a Mesoarchean metamorphic basement exists in the Yangtze Plate. Derivation of the magmatic protoliths of the biotite–tremolite schist enclaves from an oceanic crust during slab subduction, and the presence of these xenoliths within the TTG suite, indicate the existence of the initiation of plate tectonics during the Mesoarchean ( $\leq 2.94$  Ga).

**Keywords:** Archean TTG; tremolite schist; Yemadong complex; Kongling high-grade metamorphic terrane; Yangtze craton

## 1. Introduction

The two largest cratons in China, the South China Block (SCB), and the North China Craton (NCC), collided along the Qinling–Dabie–Sulu orogenic belt in the Triassic or earlier [1,2]. However, Archean rocks are relatively scarce in the SCB [3] compared with the NCC where they are widely present [4–6]. The Kongling high-grade metamorphic terrane (KHMT) is the nucleus of the Yangtze

Block, and one of just a few Archean terranes reported so far in the SCB [7–11]. Various ages for these rocks have been obtained during previous geochronological studies, especially for the TTG gneisses in the KHMT [7–10,12], but it is generally accepted that the peak period of TTG magmatism occurred at 2.90–2.85 Ga, and magmatic rocks older than 3.0 Ga are relatively rare [7,9,13,14]. Previous studies of these Archean crustal rocks in the SCB have been limited, producing just a few isolated geochemical or geochronological data [7–9,11,13,15–17]. Outcrops of Neoproterozoic and Mesoproterozoic rocks have not been directly identified in the field in the Yangtze Craton, and whether or not even more ancient rocks exist in the Yangtze Craton is a problem yet to be solved. In the absence of clear evidence from rocks in the field, the main stages of formation of the KHMT have been unclear, and this also means that issues about the early formation and evolution of the nucleus of the Yangtze Craton have remained controversial.

## 2. Geological Background and Sample Descriptions

### 2.1. Geological Background

The SCB was formed by the Grenvillian continental collision [18] of the Yangtze Craton and the Cathaysia Block. The Yangtze Craton is bounded to the west by the Songpan–Ganzi Block, to the north by the Qinling–Dabie–Sulu Orogen, and to the south by the Jiangnan Orogen (Figure 1a). The Kongling Terrane is in the northeastern part of the Yangtze Craton, has an oval dome structure, and covers an area of ~360 km<sup>2</sup> (Figure 1b). It is divided by the Wuduhe Fault into two segments known as the North Kongling Terrane, dominated by Archean TTG granitic gneisses and metasedimentary rocks (Figure 1c) [7,19], and the South Kongling Terrane, dominated by Neoproterozoic TTG intrusions such as the Huangling Dome [20–22]. Previous studies have revealed three major episodes of Archean crustal growth in the Kongling Terrane at 3.3–3.2, 2.9–2.8, and 2.7–2.6 Ga [7–9,15,19,23]. The 3.3–3.2 Ga TTG gneisses and migmatites are preserved locally in the widespread 2.9–2.8 Ga TTG rocks [7,8,19,23], and the 2.7–2.6 Ga A-type granitic gneisses, discovered recently in the eastern North Kongling Terrane, mark the termination of the subduction-related TTG magmatism and the addition of significant juvenile crustal components [15]. Crustal materials as old as 3.8 Ga have only been inferred from zircon Hf model ages [7,8], and although one 3.8 Ga detrital zircon has been reported in the Kongling Terrane from a Neoproterozoic sandstone [10], its source is uncertain.

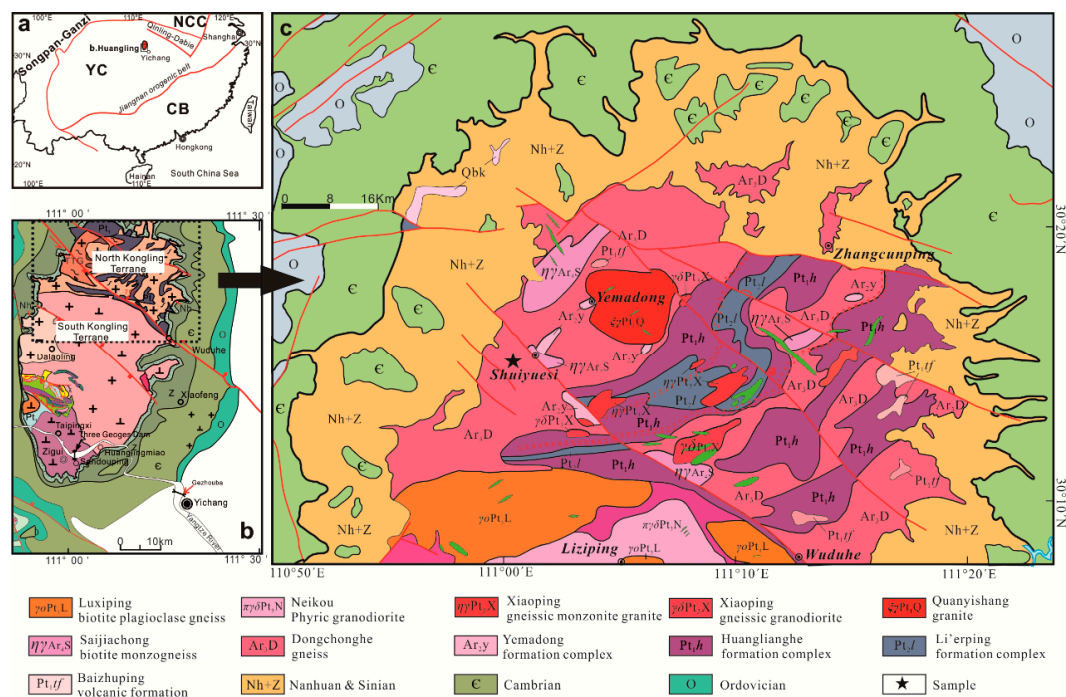


**Figure 1.** Geological map of the Archean Kongling terrane (modified from [7]). (a) Major tectonic divisions of South China. NCC denotes the North China Craton, YC denotes the Yangtze Craton, and CB denotes the Cathaysia Block; (b) Structure and division of the Kongling Terrane; (c) Geological map of the North Kongling Terrane. Star denotes the sample location.

## 2.2. Sampling

Samples D0002-1 (biotite–tremolite schist), D0002-2 (tonalitic gneiss), D0002-3 (trondhjemitic gneiss), D0002-5 (granitic gneiss), and KH110 (granitic gneiss) are fresh rock samples that were taken from a fracture surface (Figure 2a) near the Xiafangxi River ( $31^{\circ}08'25''$  N,  $111^{\circ}00'04''$  E) in the North Kongling Terrane, and we also collected one sample of fresh granitic gneiss (D0002-4) from Shuiyuesi village (on the other side of the river at  $31^{\circ}08'24''$  N,  $111^{\circ}00'05''$  E; Figure 1c). Samples SMK-1 (trondhjemitic gneiss) and SMK-4 (trondhjemitic gneiss) were collected from Shimenkou to the northwest of Wuduhe town near a streamlet ( $31^{\circ}10'11''$  N,  $111^{\circ}11'22''$  E). The exposed lithologies are mainly gray gneisses that are strongly foliated and locally migmatized with quartzofeldspathic bands and thin biotite-rich layers. The biotite–tremolite schist sample comes from an inclusion in the TTG gneiss (Figure 2a,d), and the granitic gneisses at this location form sheet-like intrusions that cut across the other TTG gneisses (Figure 2e,f). The data for other samples such as PM51-6-1, PM51-6-2, PM51-6-3, D050-1, and D050-2, included on some of the later figures, are from the unpublished data of Yunxu Wei.

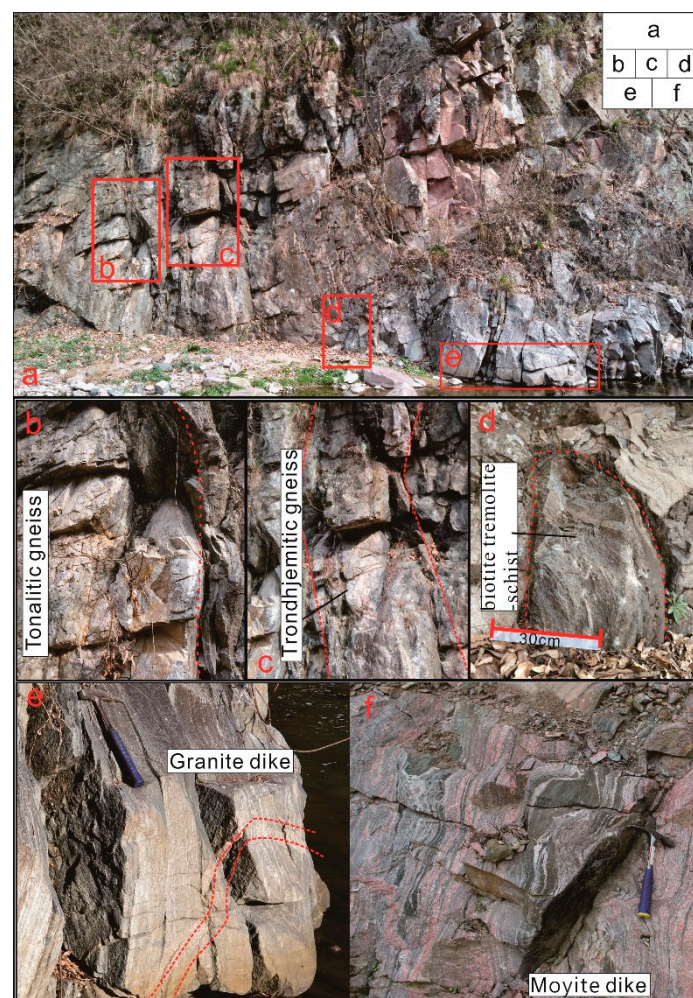


**Figure 2.** Field photographs of the Shuiyuesi granite–greenstone terrane showing outcrops of (a) the Taoyuan trondhjemitic gneiss, (b) the tonalitic gneiss, (c) the trondhjemitic gneiss, (d) the biotite–tremolite schist, (e) a granite dike, and (f) the moyite dike.



### 2.2.1. TTG

The TTG samples are medium- to fine-grained, gneissose, and composed mainly of plagioclase, quartz, K-feldspar, and biotite. The plagioclase content is 60–70%, polysynthetic twinning is visible, and the crystals show obvious K-metasomatism with visible reaction rims of K-feldspar. Most surfaces of the plagioclase are pitted with sericite and biotite alteration. Anhedral quartz makes up 10–15% of TTG rocks, and it forms irregular aggregates of granular grains in the size range of 0.2–0.8 mm. The platy biotite that makes up 5–10% of the rock occurs as dispersed grains that have been altered to muscovite and sericite. Less abundant K-feldspar and other minerals, such as epidote, are also present (Figure 3a,b).

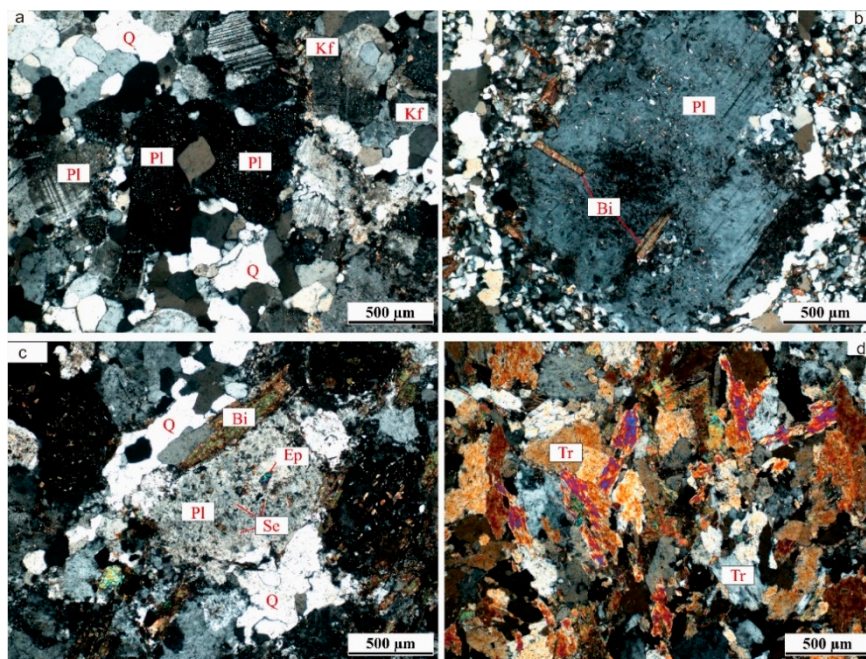


**Figure 3.** Photomicrographs of the tonalite–trondhjemite–granodiorite (TTG) gneiss and biotite–tremolite schist in the Northern Kongling Terrane. (a) Sample D0002-2; (b) Sample SMK-1; (c) Sample D0002-4; and (d) Sample D0002-1.

### 2.2.2. Granite Dikes

The granite dikes are made up of plagioclase, quartz, K-feldspar, and lesser amounts of biotite. The K-feldspar is anhedral and granular, and shows cross-hatched twinning. Sample D0002-5 underwent K-feldspathization and has a high K-feldspar content of 70%. Small amounts of epidote are also present (Figure 3c).

### 2.2.3. Biotite–Tremolite Schist

The biotite–tremolite schist has a crystalloblastic texture and schistose structure, with biotite (Bi) and tremolite (Tr) as the main minerals, along with some dolomite and magnetite. The tremolite is euhedral, columnar, and colorless, and the long axes of the crystals show a preferred orientation (Figure 3d). The tremolite grains are 0.2–2.0 mm in size and make up 60–65% of the rock. The 0.2–2.0 mm grains of biotite are euhedral, platy, and yellowish green, and they display a preferred orientation (Figure 3d). The biotite makes up about 30–35% of the rock. The 0.1–0.2 mm grains of granular dolomite fill the spaces between the tremolite and biotite. They make up 3–4% of the rock.



### 3. Analytical Methods

#### 3.1. Zircon Morphology

Sample processing for zircon separation involved crushing, initial heavy liquid separation, and subsequent magnetic separation. Representative zircons were hand-picked and mounted on adhesive tape, embedded in epoxy resin, polished to about half their size and photographed in reflected and transmitted light [24]. CL (cathode luminescence) images were used to reveal the internal structures of zircons and to help select optimum spot locations for later in situ analysis. The imaging was done at the State Key Laboratory of Continental Dynamics, Xi'an and the State Key Laboratory of Geological Processes. The laboratory in Xi'an uses a FEI Quanta 400 FEG high resolution emission field environmental scanning electron microscope connected to an Oxford INCA350 energy dispersive system (EDS, Oxford instrument, Abingdon, UK) and a Gatan Mono CL3+ system. The working distance for the CL system was 8.4 mm, while the EDS used a spot size of 6.7 nm with a voltage of 10 kV.

#### 3.2. Zircon U–Pb Dating

Laser ablation ICP-MS (Inductively Coupled Plasma Mass Spectrometry) zircon U–Pb analyses were conducted on an Agilent 7500a ICP-MS (EDS, Agilent technology co. LTD, Santa Clara, CA, USA) equipped with a 193 nm laser, which is housed at the Department of Geology, Northwest University in Xi'an, China. During analysis, the spot diameter was 30  $\mu\text{m}$ . Raw count rates for  $^{29}\text{Si}$ ,  $^{204}\text{Pb}$ ,  $^{206}\text{Pb}$ ,  $^{207}\text{Pb}$ ,  $^{208}\text{Pb}$ ,  $^{232}\text{Th}$ , and  $^{238}\text{U}$  were collected for age determination. U, Th, and Pb concentrations were calibrated by using  $^{29}\text{Si}$  as the internal calibrant and NIST 610 as the reference material. The  $^{207}\text{Pb}/^{206}\text{Pb}$ , and  $^{206}\text{Pb}/^{238}\text{U}$  ratios were calculated using the GLITTER program, which were then corrected using the Harvard zircon 91500 as external calibrant. According to the method of Ballard et al. [25] measured  $^{207}\text{Pb}/^{206}\text{Pb}$ ,  $^{206}\text{Pb}/^{238}\text{U}$ , and  $^{208}\text{Pb}/^{232}\text{Th}$  ratios in zircon 91500 were averaged over the course of the analytical session and used to calculate correction factors. These correction factors were then applied to each sample to correct for both instrumental mass bias and depth-dependent elemental and isotopic fractionation. The detailed analytical technique is described in Yuan et al. [26]. The  $^{204}\text{Pb}$  isotope cannot be precisely measured with this technique, due to a combination of low signal and interference from small amounts of  $^{204}\text{Hg}$  in the Ar gas supply. Common Pb contents were therefore evaluated using the method described by Andersen et al. [27]. The age calculations and plotting of concordia diagrams were made using ISOPLOT (ver 3.15) [28]. The errors quoted in tables and figures are at the  $2\sigma$  levels.

#### 3.3. Major and Trace Element Analyses

Whole-rock samples were crushed in a corundum jaw crusher (to a size of 60 mesh). About 60 g was powdered in an agate ring mill to a size of less than 200 mesh. Major element contents of the samples were determined by X-ray fluorescence analysis of fused glass beads using a spectrometer (3080E1; Rigaku, Tokyo, Japan) and trace elements were determined on the ICP MS (X. series, Thermo Fisher Scientific, Waltham, MA, USA) at the Wuhan Rock and Mineral Analysis Center, Ministry of Land and Resources Research, China. Analytical precision and accuracy with these methods are better than 5% for most elements. The ferric–ferrous iron proportions were determined by wet chemistry.

#### 3.4. Zircon Lu–Hf Isotope Analysis

Experiments were conducted using a Neptune Plus MC-ICP MS (Thermo Fisher Scientific, Waltham, MA, USA) in combination with a Geolas 2005 ArF-excimer laser ablation system (Lambda Physik, Göttingen, Germany) that was hosted at the state Key Laboratory of Geological Processes and Mineral Resources, China University of Geosciences in Wuhan. The energy density of laser ablation used in this study was  $5.3 \text{ J}/\text{cm}^2$ . A 'wire' signal smoothing device is included in this laser ablation system, ensuring the production of smooth signals at even very low laser repetition rates

down to 1 Hz [28,29]. Detailed operating conditions for the laser ablation system and the MC-ICP MS instrument, along with the analytical methods, are described in Hu et al. [29].

## 4. Results

### 4.1. Zircon U–Pb Ages

#### 4.1.1. Biotite–Tremolite Schist

The zircon grains from the biotite–tremolite schist (D0002-1) were subhedral to anhedral and can be classified into two types based on their CL images. Most grains show oscillatory zoning typical of magmatic zircons. The other zircon grains (red circles) display obvious metamorphic core structures (Figure 4).

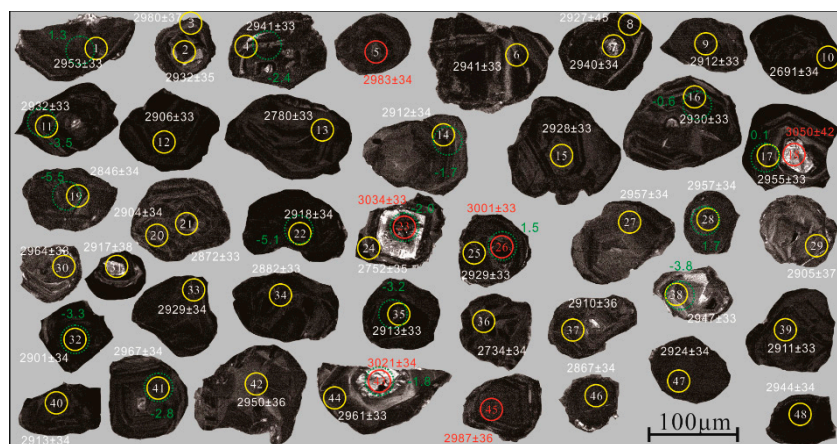


**Figure 4.** Representative cathodoluminescence images of zircons from the biotite–tremolite schist (D0002-1). The yellow circles show the locations of the LA–ICP–MS U–Pb analyses. The white number in each circle is the number of the analysis. The white number outside each circle is the age (Ma) for each site. The red circles and numbers give the analysis numbers and ages (Ma) for the smaller relict cores in those complex zircons.

Forty-eight spots on 41 grains were analyzed (Table S1, Figure 4), and 13 of the U–Pb isotopic data are discordant (Figure 5a), suggesting Pb loss caused by a later metamorphic event. These analyses, combined with six concordant spots, formed a discordia line that yielded an upper intercept  $^{207}\text{Pb}/^{206}\text{Pb}$  age of  $2994 \pm 26$  Ma ( $2\sigma$ , MSWD = 6.1,  $n = 19$ ). The six concordant spots yielded a weighted mean  $^{207}\text{Pb}/^{206}\text{Pb}$  age of  $3011 \pm 27$  Ma ( $2\sigma$ , MSWD = 2.1,  $n = 6$ ). The remaining 29 spots with ages of 2967–2901 Ma that fell close to the upper intercept were nearly concordant (concordance >98%), and gave a weighted mean  $^{207}\text{Pb}/^{206}\text{Pb}$  age of  $2933 \pm 13$  Ma ( $2\sigma$ , MSWD = 0.34,  $n = 29$ ).

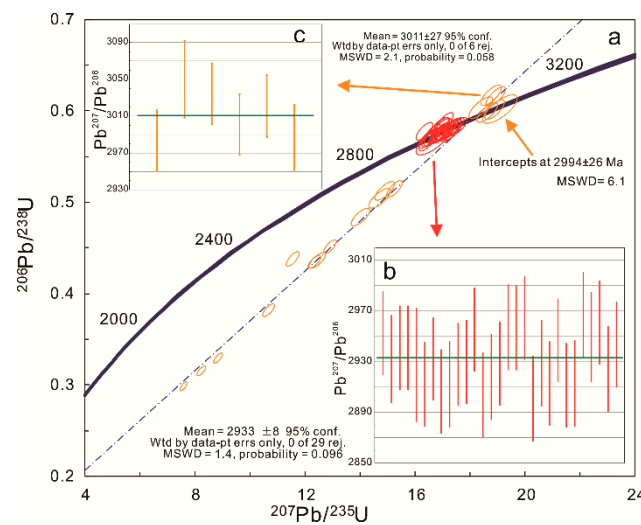


**Figure 5.** Zircon U–Pb age diagrams for the biotite–tremolite schist (D0002-1). (a) Orange circles for all analyzed spots ( $n = 19$ ) with a discordia curve that shows an upper intercept age of  $2994 \pm 26$  Ma (MSWD = 6.1). Red circles for a concordia curve ( $n = 29$ ) yield an age of  $2940 \pm 19$  Ma (MSWD = 0.42); (b) Weighted mean values for all spots with concordant ages ( $n = 29$ ). The mean age is  $2933 \pm 8$  Ma (MSWD = 1.4); (c) Weighted mean values for six spots that yield a concordant age of  $3011 \pm 27$  Ma (MSWD = 2.1).

#### 4.1.2. TTG Gneiss

The zircon grains from the tonalitic gneiss (D0002-2) have different features from the zircons of the biotite–tremolite schist sample D0002-1, described above. Thirty spots on 25 grains were analyzed (Table S2, Figure 6), and most of the U–Pb isotopic data were discordant (Figure 7). All analyzed spots gave an upper intercept age of  $2943 \pm 15$  Ma (MSWD = 8.4,  $n = 25$ ), and eight of the grains formed a tight population with a weighted mean  $^{207}\text{Pb}/^{206}\text{Pb}$  age of  $2948 \pm 26$  Ma (MSWD = 0.053,  $n = 8$ ) and a concordant age of  $2947 \pm 5.6$  Ma (MSWD = 0.006), which was within error of the U–Pb age of  $2944 \pm 22$  Ma for zircons from the biotite–tremolite schist (sample D0002-1).



**Figure 6.** Representative cathodoluminescence images of zircons from the tonalitic gneiss (D0002-2). Symbols are as in Figure 4.



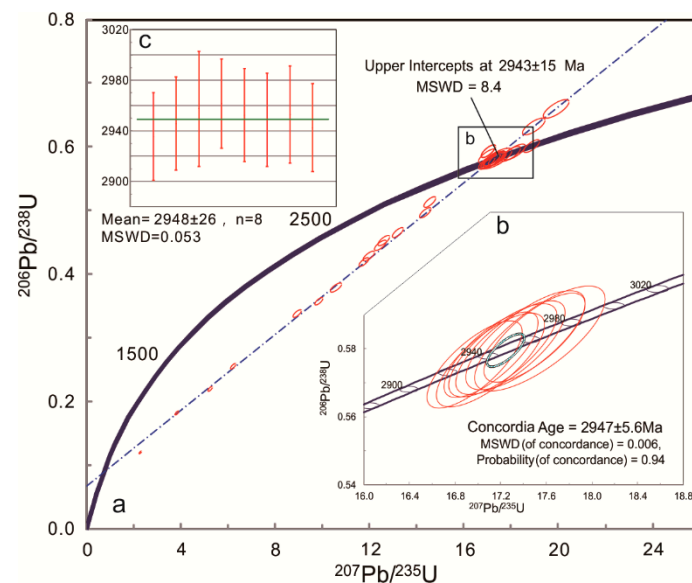


**Figure 7.** Zircon U–Pb concordia age diagram for the tonalitic gneiss (D0002-2). (a) Diagram for all analytical spots that gave a discordia line with an upper intercept  $^{207}\text{Pb}/^{206}\text{Pb}$  age of  $2943 \pm 15$  Ma; (b,c) Diagrams for eight analytical spots that gave a concordant  $^{207}\text{Pb}/^{206}\text{Pb}$  age of  $2947 \pm 5.6$  Ma and a weighted mean  $^{207}\text{Pb}/^{206}\text{Pb}$  age of  $2948 \pm 26$  Ma.

Zircon grains from the trondhjemitic gneiss (D0002-3) were euhedral to subhedral, slightly rounded in form, and display oscillatory zoning in CL images, typical of magmatic zircons (Figure 8). Most of the zircon grains displayed core–rim structures. The rims were usually very narrow, dark, and structureless, suggesting recrystallization during a later hydrothermal alteration. These rims were too narrow to be analyzed. Thirty spots on 22 grains were analyzed (Table S3), and most of the U–Pb isotopic data were discordant (Figure 9a), suggesting Pb loss caused by a later hydrothermal event. A discordia line of 14 discordant analyses yielded an upper intercept  $^{207}\text{Pb}/^{206}\text{Pb}$  age of  $3007 \pm 18$  Ma ( $2\sigma$ ,  $\text{MSWD} = 3$ ,  $n = 14$ ). The remaining 16 spots with ages of 2955–2899 Ma were nearly concordant (concordance  $>98\%$ ), and they gave a concordant age of  $^{207}\text{Pb}/^{206}\text{Pb}$  age of  $2939 \pm 4$  Ma ( $2\sigma$ ,  $\text{MSWD} = 0.18$ ,  $n = 16$ ; Figure 9b) and a weighted mean  $^{207}\text{Pb}/^{206}\text{Pb}$  age of  $2935 \pm 9$  Ma ( $2\sigma$ ,  $\text{MSWD} = 0.6$ ,  $n = 16$ ; Figure 9c).

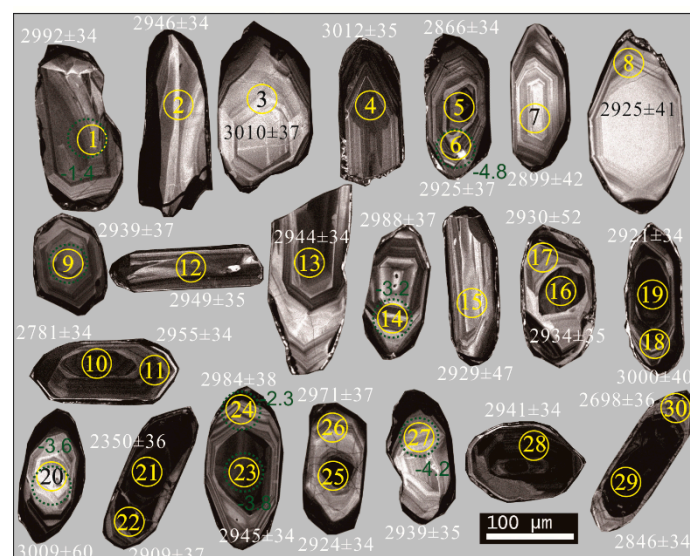


**Figure 8.** Representative cathodoluminescence images of zircons from the trondhjemitic gneiss (D0002-3). Symbols are as in Figure 4.

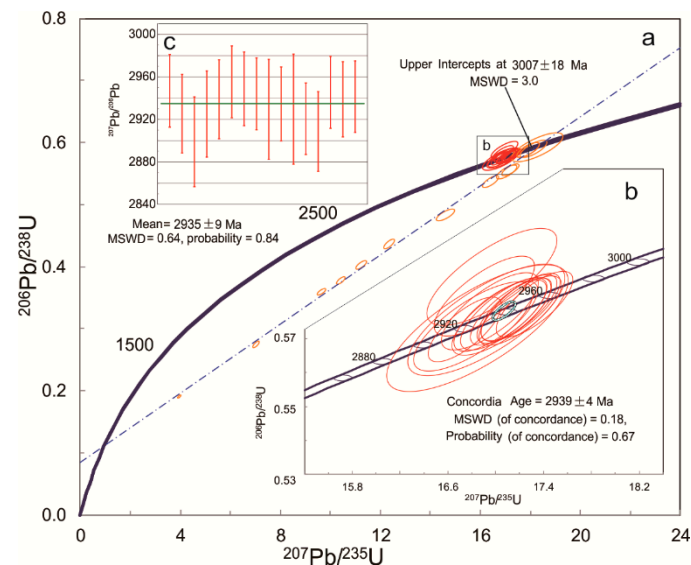


**Figure 9.** Zircon U–Pb concordia age diagrams for the trondhjemitic gneiss (D0002-3). (a) Diagram for 14 analytical spots that gave a discordia line with an upper intercept  $^{207}\text{Pb}/^{206}\text{Pb}$  age of  $3007 \pm 18$  Ma; (b,c) Diagrams for 16 analytical spots that gave a concordant  $^{207}\text{Pb}/^{206}\text{Pb}$  age of  $2939 \pm 4$  Ma and a weighted mean  $^{207}\text{Pb}/^{206}\text{Pb}$  age of  $2935 \pm 9$  Ma.

#### 4.1.3. Granite Dikes

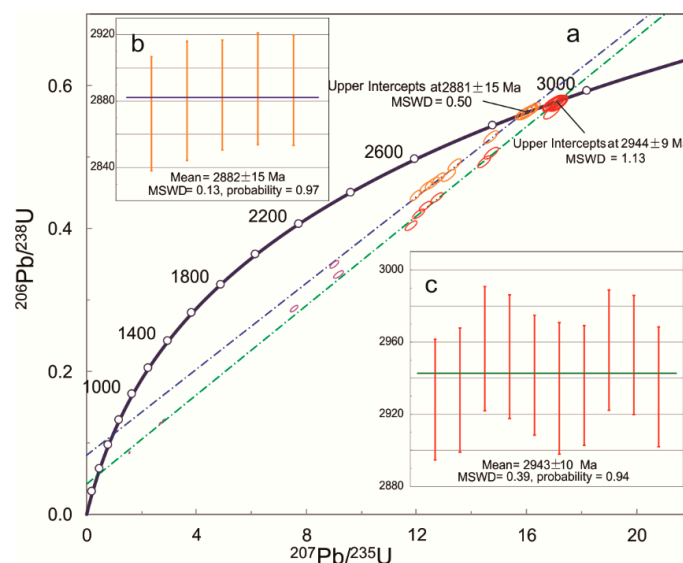
The zircon grains from the dikes of gneissic granite (D0002-4) were subhedral to anhedral (Figure 10). Most of the zircons displayed core–rim structures, and they could be divided into two groups by the internal textures of the cores. In group a, the cores had a complicated internal texture with sector zoning but no oscillatory zoning, suggesting a metamorphic origin. In contrast, the zircons of group b displayed weak sector zoning and obvious oscillatory zoning that was typical of magmatic zircons.



**Figure 10.** Representative cathodoluminescence images of zircons from the granite dike (D0002-4). Symbols are as in Figure 4. (a) Magmatic zircons with crystallization age; (b) Inheritance of zircons with metamorphic age.

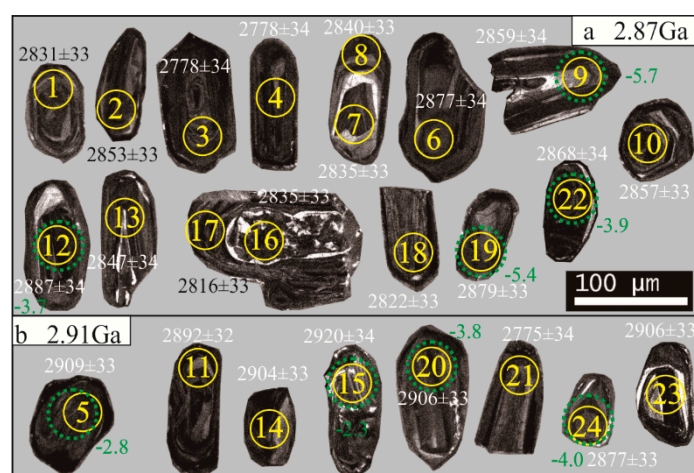
Thirty-six spots were analyzed (Table S4), and two discordia lines were present in the zircon U–Pb concordia age diagrams for sample D0002-4. The one discordia line with 18 discordant analyses yielded an upper intercept  $^{207}\text{Pb}/^{206}\text{Pb}$  age of  $2881 \pm 15$  Ma ( $2\sigma$ , MSWD = 0.50,  $n = 16$ ; Figure 11a), and five analyses gave a concordant age of  $^{207}\text{Pb}/^{206}\text{Pb}$  age of  $2882 \pm 15$  Ma ( $2\sigma$ , MSWD = 0.13,  $n = 5$ ;

Figure 11b). The other discordia line with 18 analyses defined an older upper intercept  $^{207}\text{Pb}/^{206}\text{Pb}$  age of  $2944 \pm 9$  Ma ( $2\sigma$ , MSWD = 0.5,  $n = 18$ ) and a weighted mean  $^{207}\text{Pb}/^{206}\text{Pb}$  age of  $2943 \pm 10$  Ma ( $2\sigma$ , MSWD = 0.39,  $n = 10$ ; Figure 11c).



**Figure 11.** Zircon U–Pb concordia age diagrams for the granite dike (D0002-4). (a) Diagram for all analyzed spots that gave two discordia lines with upper intercept  $^{207}\text{Pb}/^{206}\text{Pb}$  ages of  $2994 \pm 9$  Ma and  $2881 \pm 15$  Ma; (b) Diagram for five concordant analyses that gave a weighted mean  $^{207}\text{Pb}/^{206}\text{Pb}$  age of  $2882 \pm 15$  Ma; (c) Diagram for 10 concordant analyses that gave a weighted mean  $^{207}\text{Pb}/^{206}\text{Pb}$  age of  $2943 \pm 10$  Ma.

The zircon grains from the moyite dike (D0002-5; Figure 12) were smaller but otherwise similar to those from granite dike D0002-4. Twenty-four spots on 22 grains were analyzed (Table S5), and most of the U–Pb isotopic data were discordant (Figure 13a), suggesting Pb loss caused by a later hydrothermal event. A discordia line with 16 discordant analyses yielded an upper intercept  $^{207}\text{Pb}/^{206}\text{Pb}$  age of  $2874 \pm 11$  Ma ( $2\sigma$ , MSWD = 0.43,  $n = 16$ ), and another five analyses gave a concordant  $^{207}\text{Pb}/^{206}\text{Pb}$  age of  $2874 \pm 15$  Ma ( $2\sigma$ , MSWD = 0.42,  $n = 3$ ; Figure 13b). The remaining eight spots defined an older upper intercept  $^{207}\text{Pb}/^{206}\text{Pb}$  age of  $2910 \pm 11$  Ma ( $2\sigma$ , MSWD = 0.49,  $n = 8$ ) and a weighted mean  $^{207}\text{Pb}/^{206}\text{Pb}$  age of  $2911 \pm 19$  Ma ( $2\sigma$ , MSWD = 0.20,  $n = 3$ ; Figure 13c).



**Figure 12.** Representative cathodoluminescence images of zircons from the moyite dike (D0002-5). Symbols are as in Figure 4. (a) Magmatic zircons with crystallization age; (b) Inheritance of zircons with metamorphic age.



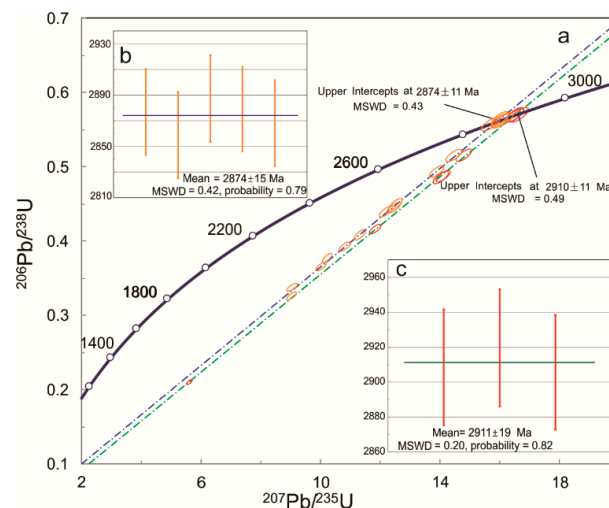


**Figure 13.** Zircon U–Pb concordia age diagrams for the moyite dike (D0002-5). (a) Diagram for all analyzed spots that gave two discordia lines with two upper intercept  $^{207}\text{Pb}/^{206}\text{Pb}$  ages of  $2910 \pm 11$  Ma and  $2874 \pm 11$  Ma; (b) Diagram for five concordant analyses that gave a weighted mean  $^{207}\text{Pb}/^{206}\text{Pb}$  age of  $2874 \pm 15$  Ma; (c) Diagram for three concordant analyses that gave a weighted mean  $^{207}\text{Pb}/^{206}\text{Pb}$  age of  $2911 \pm 19$  Ma.

#### 4.2. Whole-Rock Major and Trace Element Compositions

##### 4.2.1. Biotite-Tremolite Schist

The results of the major and trace element analyses of the five samples are presented in Table S6. The samples from the Yemadong Group displayed relatively low contents of  $\text{SiO}_2$  (30.24–54.71 wt%, average 46.23 wt%) and  $\text{Al}_2\text{O}_3$  (2.78–6.36 wt%, average 5.01 wt%), but relatively high contents of  $\text{MgO}$  (19.27–27.01 wt%, average 22.88 wt%). The samples could be divided into two series by their total alkali contents ( $\text{Na}_2\text{O} + \text{K}_2\text{O}$ ). The three samples of the first series (D050-1, D050-2, and D0002-1) had relatively high total alkali contents (1.57–3.69 wt%, average 2.86 wt%), and the other two samples displayed lower contents (0.29 wt% and 0.41 wt%).

The trace element compositions of the first series of samples (D050-1, D050-2, and D0002-1) show strong enrichments in large ion lithophile elements (LILEs; e.g., K, Rb, Ba, and Th) and depletions in high field strength elements (HFSEs; e.g., Nb, Ta, P, and Ti; Figure 14a). The other two samples show depletions in LILEs and enrichments in HFSEs. All five samples had very high Cr (>1300 ppm) and Ni (>800 ppm) contents.

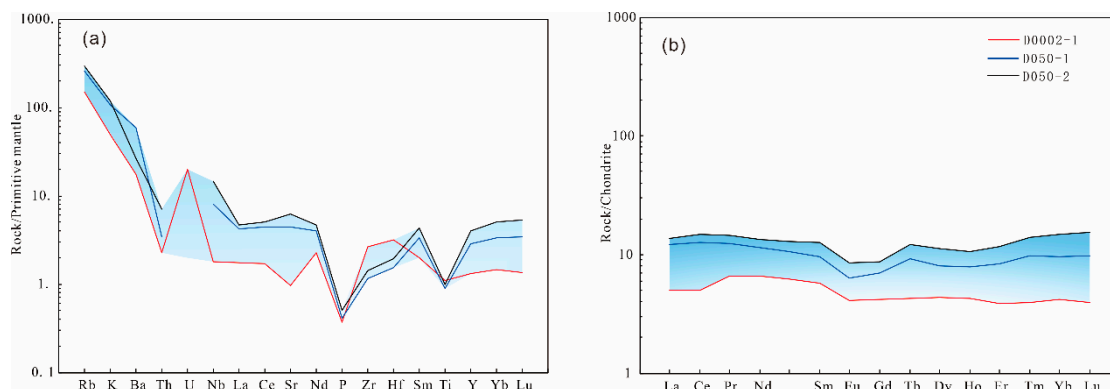


**Figure 14.** (a) Primitive-mantle-normalized trace element distributions and (b) chondrite-normalized rare earth element patterns for the biotite–tremolite schist enclaves from the Kongling Terrane. Normalizing values are from Sun and McDonough (1989) [30].

In summary, the biotite–tremolite schists possessed lower total REE values (9.46–33.12 ppm), relatively flat REE patterns (average  $(La/Yb)_N$  ratio of 0.99; Figure 14b), and both positive and negative Eu anomalies ( $\delta Eu = 0.73$ –1.40). The protoliths of the biotite–tremolite schists were basic–intermediate magmatic rocks of the calc-alkaline series, including subalkaline basalt, basalt, or basaltic andesite (Figure 15a). On a TFeO·MgO vs. SiO<sub>2</sub> volcanic rock classification diagram, all the Archean metabasite samples fell into calc-alkaline series fields.

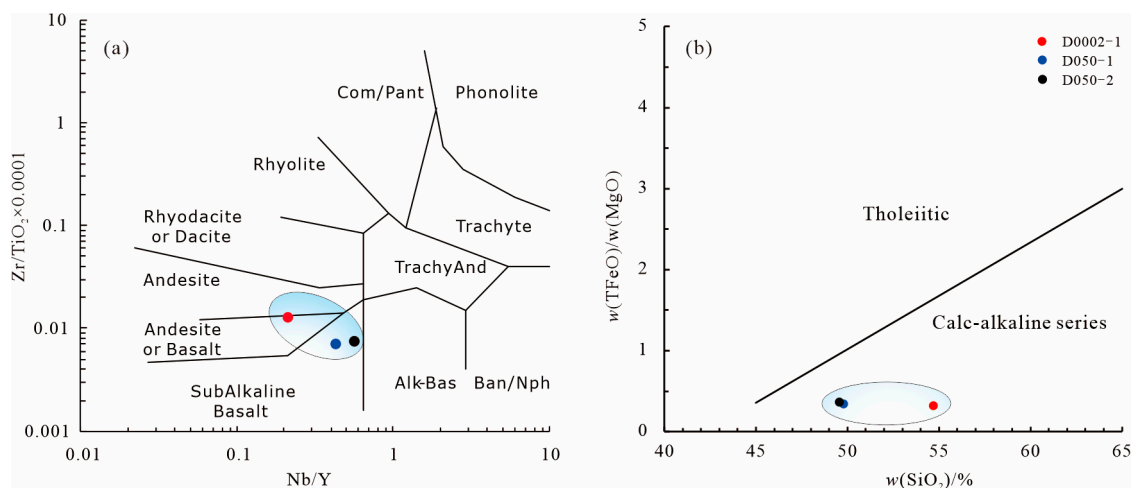


**Figure 15.** (a) Classification of the biotite–tremolite schist enclaves from the Kongling Terrane using the Nb/Y vs. Zr/Ti diagram after [31] and modified by [32] and (b) TFeO/MgO vs. SiO<sub>2</sub> diagram after [33].

#### 4.2.2. TTG Gneiss and Dikes

The major and trace element compositions of the TGG gneissic rocks are listed in Table S6. According to their normative feldspar compositions, two samples were recognized as trondhjemites, sample SMK-1 fell near the granodiorite field, and sample SMK-4 fell close to the tonalite field (Figure 16a). All the samples displayed relatively high contents of SiO<sub>2</sub> (69.79–76.80 wt%, Figure 16b), Al<sub>2</sub>O<sub>3</sub> (13.77–15.82 wt%, Figure 17), and total alkalis (Na<sub>2</sub>O + K<sub>2</sub>O; 6.51–7.37 wt%), high values of Mg<sup>#</sup> (41–47), and comparatively low contents of K<sub>2</sub>O (0.70–2.62 wt%, Figure 17), TiO<sub>2</sub> (0.09–0.43 wt%, Figure 17), FeO<sup>T</sup> (0.55–2.19 wt%, Figure 17), and MgO (0.29–1.02 wt%; Figure 17c). They are magnesian and weakly peraluminous (A/CNK 1.05–1.11; Figure 16b). In the FeOt/(FeOt+MgO)–SiO<sub>2</sub> classification diagram, and granite MALI (Modified alkali–lime index) vs. SiO<sub>2</sub> classification diagram (after [33]), they were magnesian calcic and calc-alkalic granitoids, though one sample are alkali-calcic (Figure 16c,d). These combination patterns were very similar to the typical Archean TTG pattern.

Their trace element compositions were characterized by lower total REE values (53.69–105.08 ppm), enrichments in large ion lithophile elements (LILEs), depletions in high field strength elements (HFSEs; e.g., Ti, Nb, Ta, and P), and low Cr (1.52–6.66 ppm) and Ni (2.87–4.88 ppm) contents (Figure 17a). They show moderate amounts of heavy rare earth elements (HREEs; e.g., 0.36–0.92 ppm Yb) and depletions in Eu ( $Eu/Eu^* = 1.00$ –1.52; Figure 17b; Table S6). These features make them similar to the rocks of the classic Archean TTG suite in this area [13,16,41].

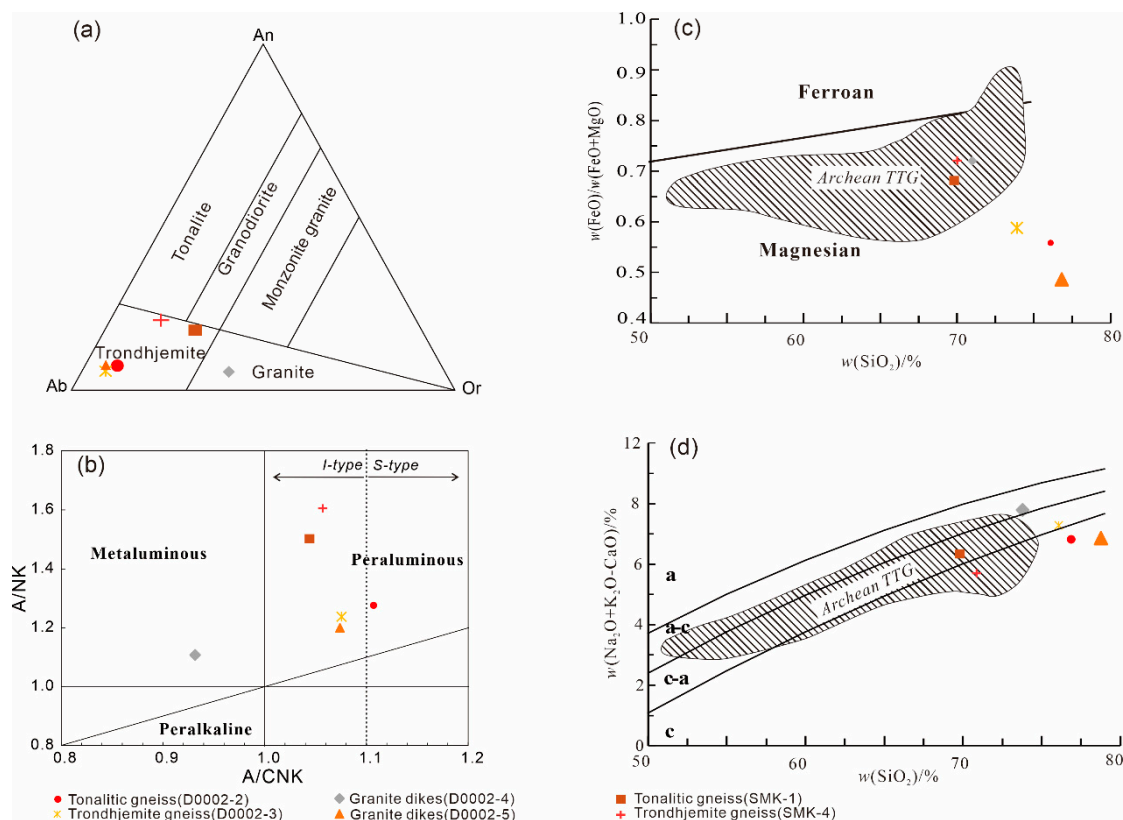


**Figure 16.** (a) The TTG suite of rocks plotted on the CIPW an–ab–or classification diagram (after [34]). An = anorthite, Ab = albite, Or = orthoclase; (b) A/NK–A/CNK diagram of granitoids (after [35]); (c)  $\text{FeO}^t/(\text{FeO}^t + \text{MgO})$ – $\text{SiO}_2$  classification diagram (after [36]); and (d) granite MALI (Modified alkali–lime index) vs.  $\text{SiO}_2$  classification diagram (after [36]). a, alkalic; a–c, alkali–calcic; c–a, calc–alkalic; c, calcic.

#### 4.2.3. Granite Dikes

The two samples of granite gneisses from the dikes plot in the granite field on a  $\text{K}_2\text{O}$  vs.  $\text{SiO}_2$  diagram with relatively high contents of  $\text{SiO}_2$  (73.97 and 78.74 wt%),  $\text{Na}_2\text{O}$  (4.41 and 5.98 wt%),  $\text{K}_2\text{O}$  (4.28 and 0.52 wt%), and  $\text{Al}_2\text{O}_3$  (13.11 and 12.85 wt%), and relatively low values of Mg# (30 and 55). The total contents of REEs were variable (443.68 and 62.35 ppm), but both samples show moderately negative Eu anomalies ( $\text{Eu}/\text{Eu}^* = 0.67$ – $0.87$ ; Figure 18b), notable depletions in Sr, P, and Eu, moderate depletions in Nb and Ta, enrichments in HFSEs (Th, U, Zr, and Hf), and alkali granite affinities (Figure 18a).

#### 4.2.4. Zircon Hf–Isotope

The zircon Lu–Hf isotopic data are given in Table S7, and the  $^{176}\text{Hf}/^{177}\text{Hf}(t)$  ratios were calculated back to their measured  $^{207}\text{Pb}/^{206}\text{Pb}$  ages. The  $\epsilon_{\text{Hf}}(t)$  values were calculated with reference to a chondritic reservoir (CHUR). The values of  $^{176}\text{Lu}/^{177}\text{Hf}$  and  $^{176}\text{Hf}/^{177}\text{Hf}$  for the CHUR were 0.0336 and 0.282785, respectively [42]. A decay constant of  $1.867 \times 10^{-5} \text{ Ma}^{-1}$  [43] was used for  $^{176}\text{Lu}$ . The single-stage model age ( $T_{\text{DM1}}$ ) was calculated relative to depleted mantle with present-day values of 0.28325 for  $^{176}\text{Hf}/^{177}\text{Hf}$  and 0.0384 for  $^{176}\text{Lu}/^{177}\text{Hf}$  [44]. The two-stage model age ( $T_{\text{DM2}}$ ), interpreted as the crust formation age, was calculated by projecting the zircon  $^{176}\text{Hf}/^{177}\text{Hf}(t)$  values back to the depleted-mantle model growth curve assuming a  $^{176}\text{Lu}/^{177}\text{Hf}$  ratio of 0.0093 for the upper continental crust [45].



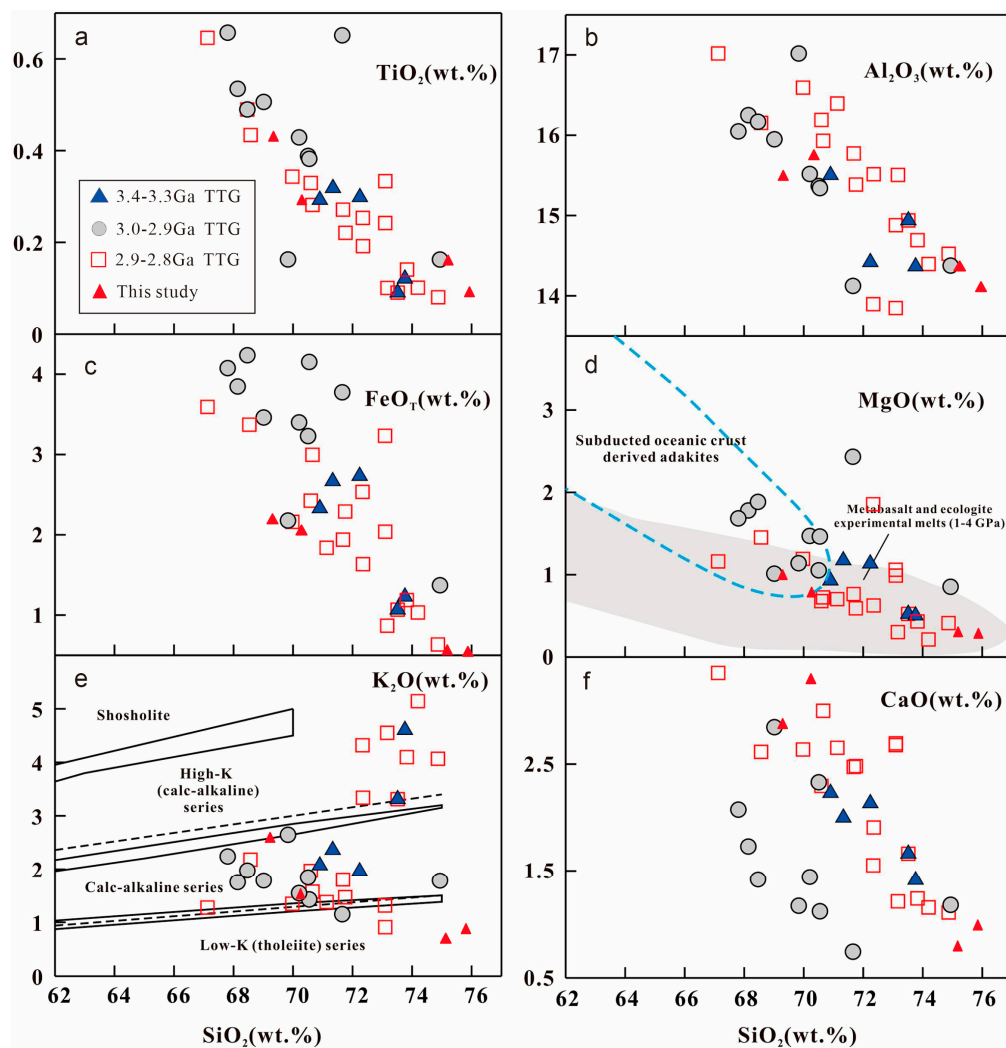


**Figure 17.** Diagrams of gneissic granitoids from the Northern Kongling Terrane, showing  $\text{SiO}_2$  vs. (a)  $\text{TiO}_2$ , (b)  $\text{Al}_2\text{O}_3$ , (c)  $\text{FeO}_T$ , (d)  $\text{MgO}$ , (e)  $\text{K}_2\text{O}$ , and (f)  $\text{CaO}$ . Symbols: blue triangles, TTGs; gray circles, biotite-granites; red squares, two-mica granites; red triangles, A-type granites. Data sources include this and previous studies ([7,13,15,19,37–40]).

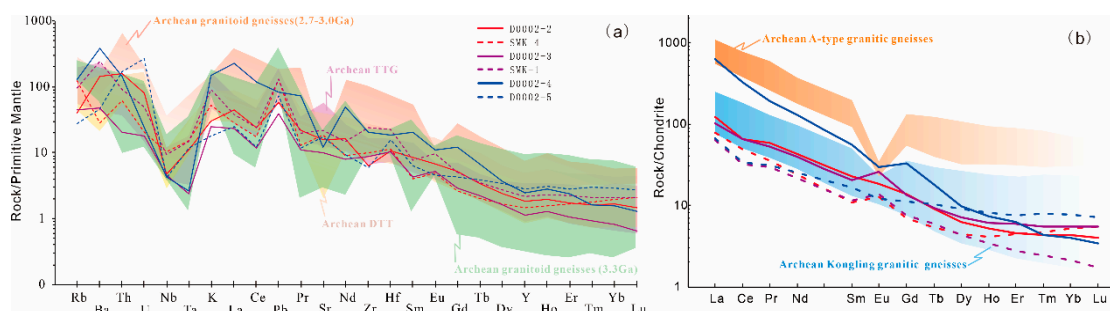


**Figure 18.** Primitive-mantle-normalized trace element distributions and chondrite-normalized rare earth element patterns in the Archean TTG and granite dikes from the Kongling terrane. Normalizing values are from [39]. The red and purple lines are for Kongling TTGs (D0002-2 and SMK-4 for tonalitic gneiss, and D0002-3 and SMK-1 for trondhjemitic gneiss), and the blue lines are for granite dikes (D0002-4 and D0002-5). Data for the Archean granitoid gneisses, Archean TTG, and Archean DTT are from Gao et al. [7], Guo et al. [13], and Guo et al. [16], respectively for the Archean TTG and granite dikes from the Kongling terrane. (a) Primitive-mantle-normalized trace element distributions diagram; (b) Chondrite-normalized rare earth element patterns diagram.

The Lu–Hf isotopes of 53 zircons from five samples were analyzed. As illustrated in Table S7, the  $^{176}\text{Hf}/^{177}\text{Hf}(t)$  ratios of the concordant zircons show two distinct groups: the biotite–tremolite schists and others. The  $^{176}\text{Hf}/^{177}\text{Hf}(t)$  ratios of the biotite–tremolite schists were higher than the ratios in the TTG gneisses and granitic dikes, ranging from 0.28077 to 0.28094 for the biotite–tremolite schists through 0.28075 to 0.28083 for the TTG gneisses and 0.28075 to 0.28085 for the granitic dikes. The  $\epsilon_{\text{Hf}}(t)$  values of concordant zircons in the biotite–tremolite schists were close to 0 but ranged from 1.8 to −5.4 (Figure 19). The concordant zircons of the five samples had  $T_{\text{DM2}}$  ages ranging from 3.56 to 3.21 Ga (Figure 20).

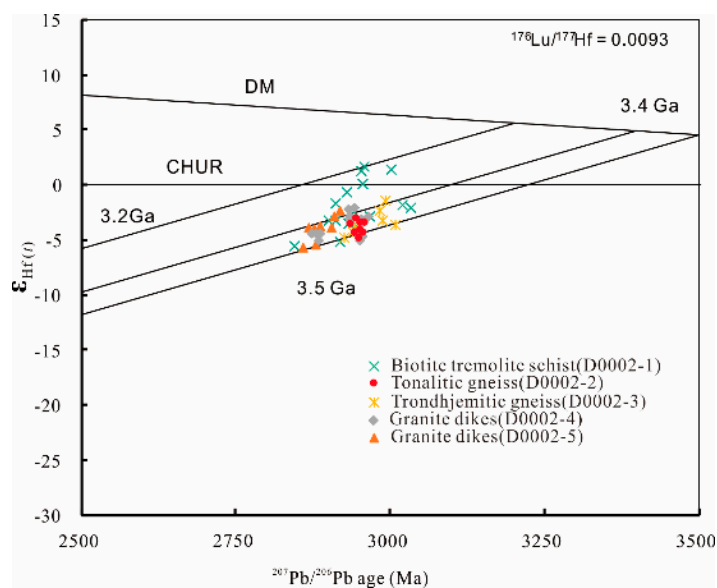


**Figure 19.**  $\epsilon_{\text{Hf}}(t)$  versus  $^{207}\text{Pb}/^{206}\text{Pb}$  zircon age diagram for the biotite–tremolite schists, tonalitic gneisses, trondhjemitic gneisses, and granitic dikes.

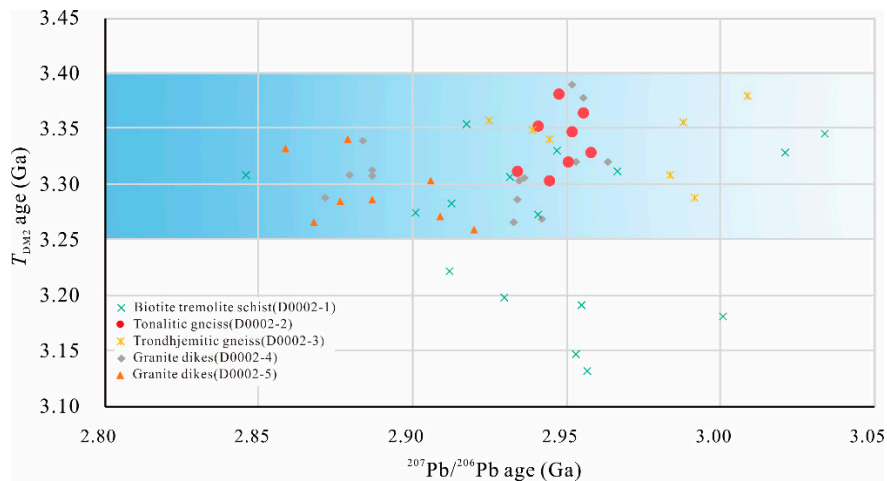


**Figure 20.**  $T_{\text{DM2}}$  age versus  $^{207}\text{Pb}/^{206}\text{Pb}$  zircon age diagram for the biotite–tremolite schists, tonalitic gneisses, trondhjemitic gneisses, and granitic dikes.

## 5. Discussion

### 5.1. Petrogenesis

#### 5.1.1. Biotite-Tremolite Schist

Although the Archean TTGs in the Kongling Terrane have been reported on and described by Guo et al. [13,16], there has been relatively little research on Archean metabasites in the Yangtze Craton [46].

We noted in section of whole-rock major and trace element compositions that all our Archean metabasite samples fell into the basaltic andesite and calc-alkaline series in the TAS volcanic rock classification. However, since the mobility of Si, Na, Ca, Rb, K, Sr, Ba, Fe, P, and Pb may have caused changes in the composition of volcanic rocks in Archean greenstone belts [47,48], we selected instead Zr, Ti, Nb, and Y for classifying these rocks, but a similar result was obtained (Figure 15). We concluded, therefore, that the protoliths of the biotite-tremolite schists were calc-alkaline basaltic andesites, and their high ratios of  $K_2O/Na_2O$  (12.8) show that they were high-K island-arc volcanic rocks, and these rocks are generally considered to form by the partial melting of subducted oceanic crust.

#### 5.1.2. TTG Magmatism

The ca. 2.9 Ga TTG gneisses are widespread in the North Kongling Terrane [7,9,15,23,39,49], and these felsic aluminous rocks are characterized by low Y (<18 ppm) and Yb (<1 ppm) contents as well as insignificant negative Eu anomalies, consistent with the definition of typical adakitic TTG rocks [50]. Typical suites of TTG and modern adakites were originally considered to result from the partial melting of a young and hot subducted oceanic crust [50,51]. Subsequent studies have shown that such rocks can also be formed by (1) fractional crystallization of mafic minerals (mainly amphibole) in hydrous basaltic magmas under high pressure [52], (2) partial melting of adakitic melt-metasomatized lithospheric mantle [53], (3) partial melting of ancient thickened lower crust [54], (4) partial melting of a delaminated lower continental crust that underwent subsequent interaction with the surrounding asthenosphere [55], or (5) partial melting of pre-existing adakitic or TTG-like (mainly tonalitic) rocks [56].

The major element compositions of the TTG samples fall close to the field of partial melts from tonalite and low-K mafic rocks as the 3.3–2.9 Ga TTGs [16] (Figure 21). They show weak Eu and Sr anomalies, low contents of HREEs (e.g., 0.36–0.92 ppm Yb), and moderate  $La_N/Yb_N$  ratios (15–29), indicating an eclogite-facies source region [57] (Figure 18). The ca. 2.9 Ga TTG gneisses also exhibited variable values of Mg# (41–47) and very low contents of Cr (1.7–12.32 ppm) and Ni (2.87–8.41 ppm), therefore, the participation of the mantle source in their genesis is unlikely. Mantle rocks in the subduction zone are enriched during slab melting, which is not consistent with the low contents of trace and rare earth elements in TTG. The geochemistry and Lu–Hf isotope characteristics of the Mesoarchean TTG suggest that their parent melt formation could have been associated with high degrees of melting of the older TTG (tonalite) associations or low-K mafic rocks (Figure 21), possibly in a subduction zone [58–60]. Mafic xenoliths or veins hosted in the ca. 2.9 Ga TTGs [39,46,61] have chemical affinities to typical island arc basalts, which lend support to an origin in a subduction setting. The possible tectonic settings include an oceanic island arc setting and a continental arc setting [39].



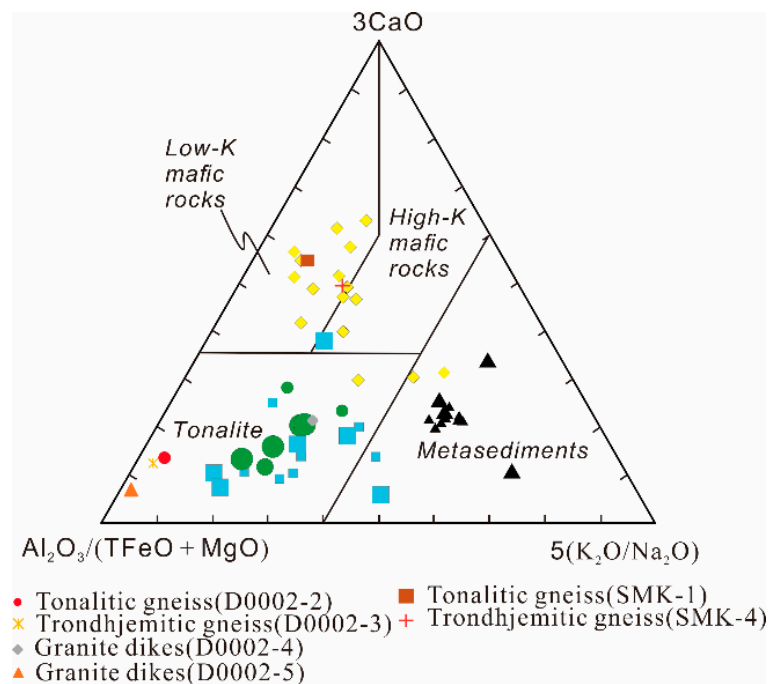


**Figure 21.** Ternary diagram of  $Al_2O_3/(TFeO + MgO)$  vs.  $3CaO$  vs.  $5(K_2O/Na_2O)$  (after Laurent et al. [62]). The different fields represent the compositions of melts derived from a range of potential sources (tonalites, metasediments, and low- and high-K mafic rocks), determined by the major-element compositions of partial melts in experimental studies (see references in Laurent et al. [62]). Symbols: diamonds = TTGs, circles = biotite granites, squares = two-mica granites, triangles = A-type granites. Data sources include this and previous studies [7,13,15,19,36–39].

In oceanic island arcs, both the subducting and the overriding plates are juvenile oceanic crust. Thus, the granitoids produced in such an environment would exhibit radiogenic Hf isotopic compositions, with depleted mantle-like  $\epsilon Hf(t)$  values [63]. This conflicts with the non-radiogenic nature of the zircons in the ca. 2.9 Ga TTG rocks, which exhibit a wide range of  $\epsilon Hf(t)$  values, but with predominantly subchondritic values (Figures 19 and 20). The  $>3.2$  Ga  $T_{DM2}$  ages and the small number of 3.2 Ga inherited zircons in the 3.0–2.9 Ga TTG gneisses [23] indicate a vital role was played by an ancient crystalline basement in the genesis of these rocks, which actually fits a continental arc setting. In continental arcs, due to the melting and/or contamination of the overriding thick ancient continental crust above the subduction zone, the granitoid magmas therein are commonly imprinted by less radiogenic Hf features and characterized by lower  $\epsilon Hf(t)$  values [64–66]. Therefore, the tectonic environment of the Kongling Terrane during the period 3.0–2.9 Ga may have been like a modern continental arc, indicating that plate tectonics in the Yangtze Craton commenced before 2.9 Ga.

Fourteen zircons from trondhjemitic gneisses containing core–rim structures yielded an upper intercept age of 3.00 Ga (Figure 18a and Table S6), and they might represent zircons inherited from their parental rocks. The Lu–Hf isotopes also provide the same  $\epsilon Hf(t)$  values and single- and two-stage model ages as the metamorphic zircon cores of the biotite–tremolite schists. All this evidence seems to be generally consistent with the proposal that the TTGs were derived from the partial melting of juvenile crust in the same subduction setting that produced the parental magmas of the metamorphosed basaltic andesite from subducted oceanic crust. These parental magmas might indeed have contributed to the juvenile crust through a process of underplating.

## 5.2. Tectonic Implications

The recently discovered biotite–tremolite schists in the Kongling Terrane, the subject of this paper, are among the oldest rocks of the Yangtze Craton. Consequently, understanding their genesis and evolution is key to understanding the initiation of plate tectonics in South China.

Two groups of zircon  $^{206}\text{Pb}/^{207}\text{Pb}$  ages were obtained from the zircons with core–rim structures of the biotite–tremolite schists, with the cores giving the older age of 3.00 Ga. Although the Th/U ratios in the cores were slightly higher than in the rims, their images were light-colored with flower shapes or cloud rings, which are characteristics of recrystallized zircons (Figure 4). The 3.00 Ga ages of the zircon cores could probably be treated as a record of early metamorphic/magmatic events. The low contents of U in the zircons might result in the metamorphic ages still falling on or near the concordant curve.

The Lu–Hf isotope data also indicate that the biotite–tremolite schists formed at around 3.00 Ga, which was the same age as shown by the metamorphic zircon cores. The single- and two-stage model ages of hafnium were 3.26 Ga and 3.39 Ga, respectively, and these ages were within error of the ages of the metamorphic zircon cores. These very close age data combined with the geochemical character of high-K island-arc volcanic rocks (in Section 5.1.1) suggest the protolith of the metamorphosed basaltic andesites were derived from the partial melting of juvenile crust in a subduction zone setting.

Apart from the magmatic events, ages of 2.93 Ga were obtained from both cores and rims. These 2.93 Ga zircons cores show dark CL images and low Th/U ratios ( $<0.1$ ), indicating that the grains underwent a metamorphic recrystallization in the presence of fluids. The rims of the zircons show uniform structures in the CL images, and they had low Th/U ratios ( $<0.1$ ). As the zircons with higher U contents displayed greater Pb loss, the data from the analytical spots fall on the discordia curve with a 2.93 Ga upper intercept age. These two important thermal events could also be observed in the age data for the zircons from the Dongchonghe TTG rocks (D0002-2 and D0002-3), which are interpreted to be the same as other tectonothermal events recorded by zircons, as described by Gao et al. [7], Qiu et al. [9], and Zhang et al. [10].

The 3.3–3.0 Ga metamorphic/magmatic events might be related to the subduction of oceanic crust that produced the trondhjemitic and the high-K calc-alkaline island-arc basaltic andesites. The 2.93–2.91 Ga ages would be related to the first metamorphic event that occurred when the TTG granites and tholeiitic basaltic rock enclaves were transformed into TTG gneisses and amphibolite enclaves, respectively, while the ~2.87 Ga alkaline magmatism was related to a regional post-orogenic extensional environment. Guo et al. [16] pointed out that the granitoid magmatism changed from TTG- to granite-dominated after 2.8 Ga, and this change may reflect a transition from subduction to collision-related events.

Taking into account the several tectonic/magmatic thermal events that have been described in the previous literature at 2.75–2.70 Ga and 2.6–2.5 Ga [61], and 2.1–1.9 Ga [12,17,67–69], our latest data show that the Yangtze continental nucleus underwent at least five widespread tectonic/magmatic thermal events during the Paleoproterozoic and the Mesoarchean.

## 6. Conclusions

(1) The ages of the early cores of zircons from the biotite–tremolite schist enclaves hosted by the TTG gneisses in the Kongling high-grade metamorphic terrane of the Yangtze Craton, China, were similar to the metamorphic recrystallization ages and model ages indicated by Hafnium isotopes (ca. 3.00 Ga), which suggests that the basaltic protoliths of these schists were formed before or close to 3.00 Ga. The data indicate that these schists represent the metamorphosed basaltic igneous rocks that formed the basal part of a Mesoarchean granite–greenstone belt.

(2) The host TTG gneisses were derived from the partial melting of subducted oceanic crust, which was consistent with the proposal that the early metamorphic/tectonic thermal events in the Yangtze continental core record the initiation of global plate tectonics at 3.00 Ga.

**Supplementary Materials:** The following are available online at <http://www.mdpi.com/2075-163X/9/11/689/s1>, Table S1: U–Pb isotopic ratios and apparent ages of zircons of the biotite tremolite-schist (D0002-1) from the Kongling complex, Table S2: U–Pb isotopic ratios and apparent ages of zircons of the tonalitic gneiss (D0002-2) from the Kongling complex, Table S3: U–Pb isotopic ratios and apparent ages of zircons of the trondjemitic gneiss (D0002-3) from the Kongling complex, Table S4: U–Pb isotopic ratios and apparent ages of zircons of the granite dikes (D0002-4), Table S5: U–Pb isotopic ratios and apparent ages of zircons of the granite dikes (D0002-5), Table S6: Results of the major and trace element analyses of samples from Shuiyuesi area, Table S7: LA-MC-ICPMS zircon Lu–Hf isotope data for the samples from Shuiyuesi area.

**Author Contributions:** Conceptualization, W.Z. and Y.W.; Data curation, W.Z., Y.W. and H.L.; Formal analysis, W.Z. and D.X.; Project administration, Y.X. and X.Z.; Resources, Z.H., X.H. and X.Z.; Writing—original draft, W.Z.; Writing—review & editing, W.Z.

**Funding:** This study is supported by the National Natural Science Foundation of China (No. 41703024) and the work items of China Geological Survey (No. DD20190374, DD20160029-02, 12120113061700).

**Acknowledgments:** Thanks to Diwu Chunrong, Liu Xiaoming and Gong Huadong from the State Key Laboratory of Continental Dynamics of Northwest University for their support and assistance on zircon U–Pb testing. Hf isotope determination was supported and assisted by Zhang Chenxi, State key laboratory of geological processes and mineral resources of China University of Geosciences. Wish to acknowledge Tan Mantang, An Zhihui, Yang Shiping, Liu Tao, etc., who participated in the field work. The authors are grateful to the critical comments from two anonymous reviewers which profoundly enhanced the quality of this manuscript.

**Conflicts of Interest:** The authors declare no conflict of interest.

## References

1. Hacker, B.R.; Ratschbacher, L.; Webb, L.; Ireland, T.; Walker, D.; Shuwen, D. U/Pb zircon ages constrain the architecture of the ultrahigh-pressure Qinling–Dabie Orogen, China. *Earth Planet. Sci. Lett.* **1998**, *161*, 215–230. [[CrossRef](#)]
2. Li, S.; Xiao, Y.; Liou, D.; Chen, Y.; Ge, N.; Zhang, Z.; Sun, S.S.; Cong, B.; Zhang, R.; Hart, S.R.; et al. Collision of the North China and Yangtze Blocks and formation of coesite-bearing eclogites: Timing and processes. *Chem. Geol.* **1993**, *109*, 89–111. [[CrossRef](#)]
3. Zhang, S.B.; Zheng, Y.F. Formation and evolution of Precambrian continental lithosphere in South China. *Gondwana Res.* **2013**, *23*, 1241–1260. [[CrossRef](#)]
4. Wu, Y.B.; Zheng, Y.F.; Gao, S.; Jiao, W.F.; Liu, Y.S. Zircon U–Pb age and trace element evidence for Paleoproterozoic granulite-facies metamorphism and Archean crustal rocks in the Dabie Orogen. *Lithos* **2008**, *101*, 308–322. [[CrossRef](#)]
5. Wu, F.Y.; Zhang, Y.B.; Yang, J.H.; Xie, L.W.; Yang, Y.H. Zircon U–Pb and Hf isotopic constraints on the Early Archean crustal evolution in Anshan of the North China Craton. *Precambrian Res.* **2008**, *167*, 339–362. [[CrossRef](#)]
6. Song, B.; Nutman, A.P.; Liu, D.; Wu, J. 3800 to 2500 Ma crustal evolution in the Anshan area of Liaoning Province, northeastern China. *Precambrian Res.* **1996**, *78*, 79–94. [[CrossRef](#)]
7. Gao, S.; Yang, J.; Hu, Z.C.; Yuan, H.L.; Gong, H.J.; Li, M.; Xiao, G.Q.; Wei, J.Q. Age and growth of the Archean Kongling terrain, South China, with emphasis on 3.3 Ga granitoid gneisses. *Geochim. Cosmochim. Acta Suppl.* **2011**, *72*, 153–182. [[CrossRef](#)]
8. Jiao, W.F.; Wu, Y.B.; Yang, S.H.; Peng, M.; Wang, J. The oldest basement rock in the Yangtze Craton revealed by zircon U–Pb age and Hf isotope composition. *Sci. China Ser. D–Earth Sci.* **2009**, *52*, 1393–1399. [[CrossRef](#)]
9. Qiu, Y.; Gao, S.; McNaughton, N.J.; Groves, D.I.; Ling, W. First evidence of >3.2Ga continental crust in the Yangtze craton of south China and its implications for Archean crustal evolution and Phanerozoic tectonics. *Geology* **2000**, *28*, 11–14. [[CrossRef](#)]
10. Zhang, S.B.; Zheng, Y.F.; Wu, Y.B.; Zhao, Z.F.; Gao, S.; Wu, F.Y. Zircon U–Pb age and Hf isotope evidence for 3.8 Ga crustal remnant and episodic reworking of Archean crust in South China. *Earth Planet. Sci. Lett.* **2006**, *252*, 56–71. [[CrossRef](#)]
11. Qiu, X.F.; Ling, W.L.; Liu, X.M.; Lu, S.S.; Jiang, T.; Wei, Y.X.; Peng, L.H.; Tan, J.J. Evolution of the Archean continental crust in the nucleus of the Yangtze block: Evidence from geochemistry of 3.0 Ga TTG gneisses in the Kongling high-grade metamorphic terrane, South China. *J. Asian Earth Sci.* **2018**, *154*, 149–161. [[CrossRef](#)]
12. Ling, W.; Gao, S.; Zheng, H.; Zhou, L.; Zhao, Z. Sm–Nd isotope geochronology of the Qiling complex in the Huangling area of the Yangtze Craton. *Chin. Sci. Bull.* **1998**, *43*, 86.

13. Guo, J.L.; Gao, S.; Wu, Y.B.; Li, M.; Chen, K.; Hu, Z.C.; Liang, Z.W.; Liu, Y.S.; Zhou, L.; Zong, K.Q.; et al. 3.45 Ga granitic gneisses from the Yangtze Craton, South China: Implications for Early Archean crustal growth. *Precambrian Res.* **2014**, *242*, 82–95. [\[CrossRef\]](#)
14. Liu, X.; Gao, S.; Diwu, C.; Ling, W. Precambrian crustal growth of Yangtze Craton as revealed by detrital zircon studies. *Am. Sci.* **2008**, *308*, 421–468.
15. Chen, K.; Gao, S.; Wu, Y.B.; Guo, J.L.; Hu, Z.C.; Liu, Y.S.; Zong, K.Q.; Liang, Z.W.; Geng, X.L. 2.6–2.7 Ga crustal growth in Yangtze craton, South China. *Precambrian Res.* **2013**, *224*, 472–490. [\[CrossRef\]](#)
16. Guo, J.L.; Wu, Y.B.; Gao, S.; Jin, Z.M.; Zong, K.Q.; Hu, Z.C.; Chen, K.; Chen, H.H.; Liu, Y.S. Episodic Paleoproterozoic–Paleoproterozoic (3.3–2.0 Ga) granitoid magmatism in Yangtze Craton, South China: Implications for late Archean tectonics. *Precambrian Res.* **2015**, *270*, 246–266. [\[CrossRef\]](#)
17. Zhang, S.B.; Zheng, Y.F.; Wu, Y.B.; Zhao, Z.F.; Gao, S.; Wu, F.Y. Zircon U–Pb age and Hf–O isotope evidence for Paleoproterozoic metamorphic event in South China. *Precambrian Res.* **2006**, *151*, 265–288. [\[CrossRef\]](#)
18. Li, Z.; Li, X.; Zhou, H.; Kinny, P.D. Grenvillian continental collision in south China: New SHRIMP U–Pb zircon results and implications for the configuration of Rodinia. *Geology* **2002**, *30*, 163–166. [\[CrossRef\]](#)
19. Gao, S.; Ling, W.L.; Qiu, Y.M.; Lian, Z.; Hartmann, G.; Simon, K. Contrasting geochemical and Sm–Nd isotopic compositions of Archean metasediments from the Kongling high-grade terrain of the Yangtze craton: Evidence for cratonic evolution and redistribution of REE during crustal anatexis. *Geochim. Cosmochim. Acta* **1999**, *63*, 2071–2088. [\[CrossRef\]](#)
20. Ling, W.; Gao, S.; Cheng, J.; Jiang, L.; Yuan, H.; Hu, Z. Neoproterozoic magmatic events within the Yangtze continental interior and along its northern margin and their tectonic implication: Constraint from the ELA–ICPMS U–Pb geochronology of zircons from the Huangling and Hannan complexes. *Acta Petrol. Sin.* **2006**, *22*, 387–396.
21. Wei, Y.X.; Peng, S.B.; Jiang, X.F.; Peng, Z.Q.; Peng, L.H.; Li, Z.H.; Zhou, P.; Zeng, X. SHRIMP zircon U–Pb ages and geochemical characteristics of the neoproterozoic granitoids in the Huangling anticline and its tectonic setting. *J. Earth Sci.* **2012**, *23*, 659–676. [\[CrossRef\]](#)
22. Zhang, S.B.; Zheng, Y.F.; Zhao, Z.F.; Wu, Y.B.; Yuan, H.; Wu, F.Y. Neoproterozoic anatexis of Archean lithosphere: Geochemical evidence from felsic to mafic intrusions at Xiaofeng in the Yangtze Gorge, South China. *Precambrian Res.* **2008**, *163*, 210–238. [\[CrossRef\]](#)
23. Zhang, S.B.; Zheng, Y.F.; Wu, Y.B.; Zhao, Z.F.; Gao, S.; Wu, F.Y. Zircon isotope evidence for  $\geq 3.5$  Ga continental crust in the Yangtze craton of China. *Precambrian Res.* **2006**, *146*, 16–34. [\[CrossRef\]](#)
24. Song, B.; Zhang, Y.H.; Wan, Y.S.; Jian, P. Mount making and procedure of shrimp dating. *Geol. Rev.* **2002**, *48*, 26–30.
25. Ballard, J.R.; Palin, J.M.; Williams, I.S.; Campbell, I.H.; Faunes, A. Two ages of porphyry intrusion resolved for the super-giant Chuquibambilla copper deposit of northern Chile by ELA–ICP–MS and SHRIMP. *Geology* **2001**, *29*, 383–386. [\[CrossRef\]](#)
26. Yuan, H.; Gao, S.; Liu, X.; Li, H.; Günther, D.; Wu, F. Accurate U–Pb age and trace element determinations of zircon by laser ablation–inductively coupled plasma–mass spectrometry. *Geostand. Geoanalytical Res.* **2004**, *28*, 353–370. [\[CrossRef\]](#)
27. Andersen, T. Correction of common lead in U–Pb analyses that do not report  $^{204}\text{Pb}$ . *Chem. Geol.* **2002**, *192*, 59–79. [\[CrossRef\]](#)
28. Ludwig, K.R. Isoplot 3.00: A geochronological toolkit for Microsoft Excel. *Berkeley Geochronol. Cent. Spec. Publ.* **2003**, *4*, 1–70.
29. Hu, Z.; Liu, Y.; Gao, S.; Liu, W.; Zhang, W.; Tong, X.; Lin, L.; Zong, K.; Li, M.; Chen, H. Improved in situ Hf isotope ratio analysis of zircon using newly designed X skimmer cone and jet sample cone in combination with the addition of nitrogen by laser ablation multiple collector ICP–MS. *J. Anal. At. Spectrom.* **2012**, *27*, 1391–1399. [\[CrossRef\]](#)
30. Sun, S.S.; McDonough, W.F. Chemical and isotopic systematic of oceanic basalts: Implication and processes/Magmatism in the Ocean Basins. *Geological Soc. Lond. Spec. Publ.* **1989**, *42*, 313–345. [\[CrossRef\]](#)
31. Hu, Z.; Liu, Y.; Gao, S.; Xiao, S.; Zhao, L.; Günther, D.; Li, M.; Zhang, W.; Zong, K. A “wire” signal smoothing device for laser ablation inductively coupled plasma mass spectrometry analysis. *Spectrochim. Acta Part B At. Spectrosc.* **2012**, *78*, 50–57. [\[CrossRef\]](#)
32. Winchester, J.A.; Floyd, P.A. Geochemical discrimination of different magma series and their differentiation products using immobile elements. *Chem. Geol.* **1977**, *20*, 325–343. [\[CrossRef\]](#)



33. Pearce, J.A. A user's guide to basalt discrimination diagrams. In *Trace Element Geochemistry of Volcanic Rocks: Applications for Massive Sulphide Exploration*; Geological Association of Canada: Toronto, ON, Canada, 1996; Volume 12, pp. 79–113.
34. Miyashiro, A. Volcanic rock series in island arcs and active continental margins. *Am. J. Sci.* **1974**, *274*, 321–355. [[CrossRef](#)]
35. O'Connor, J. A classification for quartz-rich igneous rocks based on feldspar ratios. *Geol. Surv. Prof. Pap.* **1965**, *525*, 79–84.
36. Maniar, P.D.; Piccoli, P.M. Tectonic discrimination of granitoids. *Geol. Soc. Am. Bull.* **1989**, *101*, 635–643. [[CrossRef](#)]
37. Frost, B.R.; Barnes, C.G.; Collins, W.J.; Arculus, R.J.; Ellis, D.J.; Frost, C.D. A geochemical classification for granitic rocks. *J. Petrol.* **2001**, *42*, 2033–2048. [[CrossRef](#)]
38. Peng, M.; Wu, Y.; Gao, S.; Zhang, H.; Wang, J.; Liu, X.; Gong, H.; Zhou, L.; Hu, Z.; Liu, Y.; et al. Geochemistry, zircon U–Pb age and Hf isotope compositions of Paleoproterozoic aluminous A-type granites from the Kongling terrain, Yangtze Block: Constraints on petrogenesis and geologic implications. *Gondwana Res.* **2012**, *22*, 140–151. [[CrossRef](#)]
39. Xiong, Q.; Zheng, J.P.; Yu, C.M.; Su, Y.P.; Tang, H.Y.; Zhang, Z.H. Zircon U–Pb age and Hf isotope of Quanyishang A-type granite in Yichang: Signification for the Yangtze continental cratonization in Paleoproterozoic. *Chin. Sci. Bull.* **2009**, *54*, 436–446. [[CrossRef](#)]
40. Li, L.; Lin, S.; Davis, D.W.; Xiao, W.; Xing, G.; Yin, C. Geochronology and geochemistry of igneous rocks from the Kongling terrane: Implications for Mesoarchean to Paleoproterozoic crustal evolution of the Yangtze Block. *Precambrian Res.* **2014**, *255*, 30–47. [[CrossRef](#)]
41. Gao, S.; Zhang, B.R. Discovery of the Archean TTG gneiss in the northern part of the Yangtze platform and its significance. *Earth Sci.–J. China Univ. Geosci.* **1990**, *15*, 675–679.
42. Bouvier, A.; Vervoort, J.D.; Patchett, P.J. The Lu–Hf and Sm–Nd isotopic composition of CHUR: Constraints from unequilibrated chondrites and implications for the bulk composition of terrestrial planets. *Earth Planet. Sci. Lett.* **2008**, *273*, 48–57. [[CrossRef](#)]
43. Söderlund, U.; Patchett, P.J.; Vervoort, J.D.; Isachsen, C.E. The <sup>176</sup>Lu decay constant determined by Lu–Hf and U–Pb isotope systematics of Precambrian mafic intrusions. *Earth Planet. Sci. Lett.* **2004**, *219*, 311–324. [[CrossRef](#)]
44. Griffin, W.L.; Wang, X.; Jackson, S.E.; Pearson, N.J.; O'Reilly, S.Y.; Xu, X.; Zhou, X. Zircon chemistry and magma mixing, SE China: In-situ analysis of Hf isotopes, Tonglu and Pingtan igneous complexes. *Lithos* **2002**, *61*, 237–269. [[CrossRef](#)]
45. Vervoort, J.D.; Patchett, P.J. Behavior of hafnium and neodymium isotopes in the crust: Constraints from Precambrian crustally derived granites. *Geochim. Cosmochim. Acta* **1996**, *60*, 3717–3733. [[CrossRef](#)]
46. Wei, J.Q.; Jing, M.M. Chronology and geochemistry of amphibolites from the Kongling complex. *Chin. J. Geol.* **2013**, *48*, 970–983.
47. Polat, A.; Hofmann, A. Alteration and geochemical patterns in the 3.7–3.8 Ga Isua greenstone belt, West Greenland. *Precambrian Res.* **2003**, *126*, 197–218. [[CrossRef](#)]
48. Polat, A.; Hofmann, A.; Rosing, M.T. Boninite-like volcanic rocks in the 3.7–3.8 Ga Isua greenstone belt, West Greenland: Geochemical evidence for intra-oceanic subduction zone processes in the early Earth. *Chem. Geol.* **2002**, *184*, 231–254. [[CrossRef](#)]
49. Zheng, J.; Griffin, W.; O'Reilly, S.Y.; Zhang, M.; Pearson, N.; Pan, Y. Widespread Archean basement beneath the Yangtze craton. *Geology* **2006**, *34*, 417–420. [[CrossRef](#)]
50. Defant, M.J.; Drummond, M.S. Derivation of some modern arc magmas by melting of young subducted lithosphere. *Nature* **1990**, *347*, 662. [[CrossRef](#)]
51. Barker, F.; Arth, J.G. Generation of trondhjemitic-tonalitic liquids and Archean bimodal trondhjemitic-basalt suites. *Geology* **1976**, *4*, 596–600. [[CrossRef](#)]
52. Castillo, P.R. An overview of adakite petrogenesis. *Chin. Sci. Bull.* **2006**, *51*, 257–268. [[CrossRef](#)]
53. Gao, Y.; Yang, Z.; Santosh, M.; Hou, Z.; Wei, R.; Tian, S. Adakitic rocks from slab melt-modified mantle sources in the continental collision zone of southern Tibet. *Lithos* **2010**, *119*, 651–663. [[CrossRef](#)]
54. Chung, S.L.; Liu, D.; Ji, J.; Chu, M.F.; Lee, H.Y.; Wen, D.J.; Lo, C.H.; Lee, T.Y.; Qian, Q.; Zhang, Q. Adakites from continental collision zones: Melting of thickened lower crust beneath southern Tibet. *Geology* **2003**, *31*, 1021–1024. [[CrossRef](#)]

55. Gao, S.; Rudnick, R.L.; Yuan, H.L.; Liu, X.M.; Liu, Y.S.; Xu, W.L.; Ling, W.L.; Ayers, J.; Wang, X.C.; Wang, Q.H. Recycling lower continental crust in the North China craton. *Nature* **2004**, *432*, 892–897. [[CrossRef](#)] [[PubMed](#)]
56. Moyen, J.F. High Sr/Y and La/Yb ratios: The meaning of the “adakitic signature”. *Lithos* **2009**, *112*, 556–574. [[CrossRef](#)]
57. Moyen, J.F. The composite Archaean grey gneisses: Petrological significance, and evidence for a non-unique tectonic setting for Archaean crustal growth. *Lithos* **2011**, *123*, 21–36. [[CrossRef](#)]
58. Martin, H.; Moyen, J.F. Secular changes in tonalite–trondhjemite–granodiorite composition as markers of the progressive cooling of Earth. *Geology* **2002**, *30*, 319–322. [[CrossRef](#)]
59. Martin, H.; Smithies, R.; Rapp, R.; Moyen, J.F.; Champion, D. An overview of adakite, tonalite–trondhjemite–granodiorite (TTG), and sanukitoid: Relationships and some implications for crustal evolution. *Lithos* **2005**, *79*, 1–24. [[CrossRef](#)]
60. Moyen, J.F.; Martin, H. Forty years of TTG research. *Lithos* **2012**, *148*, 312–336. [[CrossRef](#)]
61. Wei, J.; Wang, J. Zircon age and Hf isotope compositions of amphibolite enclaves from the Kongling complex. *Geol. J. China Univ.* **2012**, *18*, 589–600.
62. Laurent, O.; Martin, H.; Moyen, J.F.; Doucelance, R. The diversity and evolution of late-Archaean granitoids: Evidence for the onset of “modern-style” plate tectonics between 3.0 and 2.5 Ga. *Lithos* **2014**, *205*, 208–235. [[CrossRef](#)]
63. Schaltegger, U.; Zeilinger, G.; Frank, M.; Burg, J.P. Multiple mantle sources during island arc magmatism: U–Pb and Hf isotopic evidence from the Kohistan arc complex, Pakistan. *Terra Nova* **2002**, *14*, 461–468. [[CrossRef](#)]
64. Ducea, M.N.; Saleeby, J.B.; Bergantz, G. The Architecture, Chemistry, and Evolution of Continental Magmatic Arcs. *Annu. Rev. Earth Planet. Sci.* **2015**, *43*, 299–331. [[CrossRef](#)]
65. Jones, R.E.; Kirstein, L.A.; Kasemann, S.A.; Dhuime, B.; Elliott, T.; Litvak, V.D.; Alonso, R.; Hinton, R.; Facility, E.I.M. Geodynamic controls on the contamination of Cenozoic arc magmas in the southern Central Andes: Insights from the O and Hf isotopic composition of zircon. *Geochim. Cosmochim. Acta* **2015**, *164*, 386–402. [[CrossRef](#)]
66. Li, Z.X.; Li, X.H.; Chung, S.L.; Lo, C.H.; Xu, X.; Li, W.X. Magmatic switch-on and switch-off along the South China continental margin since the Permian: Transition from an Andean-type to a Western Pacific-type plate boundary. *Tectonophysics* **2012**, *532*, 271–290. [[CrossRef](#)]
67. Han, Q.S.; Peng, S.B.; Polat, A.; Kusky, T.; Deng, H.; Wu, T.Y. A ca.2.1 Ga Andean-type margin built on metasomatized lithosphere in the northern Yangtze craton, China: Evidence from high-Mg basalts and andesites. *Precambrian Res.* **2017**, *309*, 309–324. [[CrossRef](#)]
68. Ling, W.L.; Gao, S. The tectonic thermal events and the evolution in the late Paleoproterozoic of the Yangtze craton in the Yangtze. *Chin. Sci. Bull.* **2000**, *45*, 2343–2347.
69. Peng, S.; Han, Q.; Polat, A.; Kusky, T.M. The discovery of Paleoproterozoic ophiolitic melange in the northern part of the Huangling Dome of the Yangtze Craton. *J. Earth Sci.* **2016**, *41*, 2117–2118.

